Geophysical Research Letters

RESEARCH LETTER
10.1029/2023GL105548

Key Points:

- Wind structure in the hurricane boundary layer shows significant asymmetries over water and at landfall
- The nature of these asymmetries changes significantly during landfall
- Aircraft observations of these changing asymmetries support recent modeling studies and point toward physical processes for their evolution

Correspondence to:

R. F. Rogers,
robert.rogers@noaa.gov

Citation:

Rogers, R. F., & Zhang, J. A. (2023). Airborne Doppler radar observations of tropical cyclone boundary layer kinematic structure and evolution during landfall. *Geophysical Research Letters*, *50*, e2023GL105548. https://doi.org/10.1029/2023GL105548

Received 18 JUL 2023
Accepted 29 SEP 2023

Author Contributions:

Conceptualization: Robert F. Rogers
Formal analysis: Jun A. Zhang
Investigation: Robert F. Rogers
Methodology: Robert F. Rogers, Jun A. Zhang
Software: Jun A. Zhang
Visualization: Jun A. Zhang
Writing – original draft: Robert F. Rogers
Writing – review & editing: Robert F. Rogers, Jun A. Zhang

Airborne Doppler Radar Observations of Tropical Cyclone Boundary Layer Kinematic Structure and Evolution During Landfall

Robert F. Rogers[1] and Jun A. Zhang[1,2]

[1]Atlantic Oceanographic and Meteorological Laboratory, Hurricane Research Division, NOAA, OAR, Miami, FL, USA, [2]Cooperative Institute for Marine and Atmospheric Studies, University of Miami, Miami, FL, USA

Abstract Airborne Doppler radar observations of the wind field in the tropical cyclone boundary layer (TCBL) during the landfall of Hurricane Ida (2021) are examined here. Asymmetries in tangential and radial flow are governed by tropical cyclone (TC) motion and vertical wind shear prior to landfall, while frictional effects dominate the asymmetry location during landfall. Strong TCBL inflow on the offshore-flow side of Ida occurs during landfall, while the location of the peak tangential wind at the top of the TCBL during this period is located on the onshore-flow side. A comparison of these observations with a numerical simulation of TC landfall shows many consistencies with the modeling study, though there are some notable differences that may be related to differences in the characteristics of the land surface between the simulation and the observations here.

Plain Language Summary The structure of the wind field in the lowest levels of a hurricane when it makes landfall plays a significant role in determining damage. This study uses aircraft observations to document the changes that occur in the winds in the lowest levels of a hurricane prior to and as it makes landfall. The location of the strongest inflow into the storm center and winds around the center are determined by characteristics like storm motion and environmental winds when the storm is over open water, but at landfall these wind peaks are dominated by the differences in friction between the land surface and water. At landfall, the inflow near the surface is strongest on the side of the hurricane experiencing offshore flow, while winds moving around the storm center a few thousand feet above the surface are strongest on the side experiencing onshore flow. These results are mostly consistent with computer modeling studies, allowing for studies on physical processes to be conducted using these models.

1. Introduction

The wind field in the tropical cyclone (TC) boundary layer (BL) determines the magnitude and distribution of surface enthalpy and momentum fluxes, which determines whether or not a TC will intensify (Cione et al., 2013; Emanuel, 1986, 1995, 1999; Jaimes et al., 2015; Ooyama, 1969; Shay et al., 2000; Wadler et al., 2021; Zhang et al., 2017) and governs storm surge, wind damage, and rainfall fields at landfall. Decomposing the total flow field into tangential and radial components yields important insights into physical processes governing intensity change, such as the radial advection of angular momentum and radial mass flux within and above the frictional inflow layer, as well as factors affecting the wind structure in the tropical cyclone boundary layer (TCBL), such as the azimuthal distribution of supergradient flow and the presence of TCBL jets (Smith & Montgomery, 2016; Smith et al., 2009, 2021).

Past observational and modeling studies have characterized the symmetric (i.e., azimuthally averaged) structures of TCBL flow over the open ocean (Ahern et al., 2019; Bell & Montgomery, 2008; Bryan, 2012; Kepert, 2001; Kepert & Wang, 2001; Ming et al., 2015; Montgomery et al., 2014; Rogers et al., 2012; Sanger et al., 2014; Zhang et al., 2011, 2015, 2017, 2023), finding that inflow is maximized in the lowest 200 m, with a region of weaker inflow at the top of and above the TCBL. Using composites of ~800 dropsondes from multiple hurricanes, Zhang et al. (2011) proposed a kinematic definition of the BL height based on the depth of the inflow layer, finding that the depth of the inflow layer increases from ~500 m at the radius of maximum wind (RMW) to 1,500 m at 5x RMW. Peak tangential wind occurs in the inflow layer, and there is a region of supergradient flow at and inside the region of strongest inflow.

Azimuthal asymmetries are often a significant contributor to the TCBL wind field. The dominant drivers of TCBL wind asymmetries over the open ocean are TC motion (Shapiro, 1983, Ueno & Bessho, 2011; Uhlhorn et al., 2014; Zhang & Uhlhorn, 2012) and vertical wind shear (Klotz & Jiang, 2017; Ming et al., 2022; Reasor et al., 2013; Rogers & Uhlhorn, 2008; Sun et al., 2019; Uhlhorn et al., 2014; Zhang et al., 2013). TC motion establishes a region of strong TCBL tangential flow to the right of storm motion (northern hemisphere) and maxima in radial inflow and convergence in the TCBL in the front and front-right quadrants (Shapiro, 1983). Vertical shear establishes peak tangential wind speed, inflow, and convergence in the downshear and downshear-left quadrants (Reasor et al., 2013; Uhlhorn et al., 2014; Zhang et al., 2013).

Several observational studies have examined the variation of the TCBL wind field and features at and after landfall. Giammanco et al. (2012) found the maximum BL wind scaled by the mean BL wind and low-level ($z < 300$ m) wind shear are larger in an offshore regime in the eyewall region than onshore. Roll-like features were documented during TC landfalls using Doppler radar and tower data (e.g., Kosiba & Wurman, 2014; Lorsolo et al., 2008; Wurman & Winslow, 1998; Zhu et al., 2010). Ming et al. (2014) observed enhancement of turbulence kinetic energy by convective downdrafts in the BL of outer rainbands in Typhoon Morakot (2009). The strongest surface winds during the landfall of Hurricane Harvey (2017) were also found to be associated with convective perturbations in the eyewall (Alford et al., 2019). Alford et al. (2020) investigated the coastal transition of vertical wind profiles in the BL of Hurricane Irene (2011) and found that the tangential wind maximum was within the inflow layer over water but was above the inflow layer onshore. The height of the maximum radial wind increases from water to land in response to the growth of the internal BL that forms in the transition zone due to flow adjustment to the surface roughness change (Alford et al., 2020; Hirth et al., 2012).

Variations in surface roughness dominate the creation of asymmetries near landfall. It is important to understand how these asymmetries affect the wind field in the TCBL at landfall, as these structures are what determine the hazards driven by wind, storm surge, and rainfall. A recent paper by Hlywiak and Nolan (2022, hereafter HN22) examined the structure and evolution of asymmetries in the TCBL wind field in a storm-relative framework prior to and during landfall using an idealized modeling framework. In their simulation they found an increase in the strength of the radial inflow on the offshore flow side of the TC, beginning when the TC was about 200 km offshore. They attributed the increase in radial inflow to the sudden decrease in frictional stress once the agradient offshore flow crossed the coastline and reached water. An enhanced advection of angular momentum by the secondary circulation, tied to the strengthened radial inflow in the TCBL on the offshore flow side, additionally forced a strengthening of a supergradient jet near the top of the TCBL, resulting in a maximum in wind speed downstream; that is, on the onshore flow side at the top of the TCBL. They compared some of their modeling results to a set of buoy observations of near-surface inflow angle from three landfalling TCs and found general agreement with their results.

The comparisons with observations from HN22 were limited, however, to a relatively small number of point observations at the surface, with no information on the variation of the tangential and radial flow with height and as a function of distance from the storm center. A comparison of the three-dimensional structure of the flow field in the TCBL, and its variation between when a TC is well offshore and when it is making landfall, would provide a more robust evaluation of HN22's results. Ground-based radar could provide such a comparison, but the elevation of the beam and curvature of the Earth would prevent observations of the wind field in the lowest 1–2 km, except when the TC is close (<100 km) to the radar site.

Airborne Doppler radar data, by contrast, can provide a comprehensive depiction of the structure and evolution of the flow field by sampling the TC at many different periods during its approach to landfall. In this study, profile analyses (e.g., Rogers et al., 2012; Zhang et al., 2023) from airborne Doppler radar (often referred to as the Tail Doppler Radar, or TDR) onboard the NOAA WP-3D aircraft (hereafter P-3) are used to produce analyses of tangential and radial wind in a narrow (~10-km wide) swath under the aircraft with 150 m spacing in the vertical and down to altitudes as low as 150 m above the surface. Additionally, three-dimensional TDR analyses that provide winds and reflectivity in a swath extending approximately 50 km in either direction normal to the flight track, with 500 m spacing in the vertical, will be used. Together, these radar analyses will be used to examine the structure of TCBL tangential and radial flow in Hurricane Ida as it made landfall along the coastline of Louisiana in August 2021. The analysis shown here will provide an opportunity to evaluate results from HN22 in a more comprehensive and robust manner than what was shown in their study. It will also provide the opportunity to assess the evolution of TCBL flow fields as Ida transitioned from an over-water exposure to one associated with landfall.

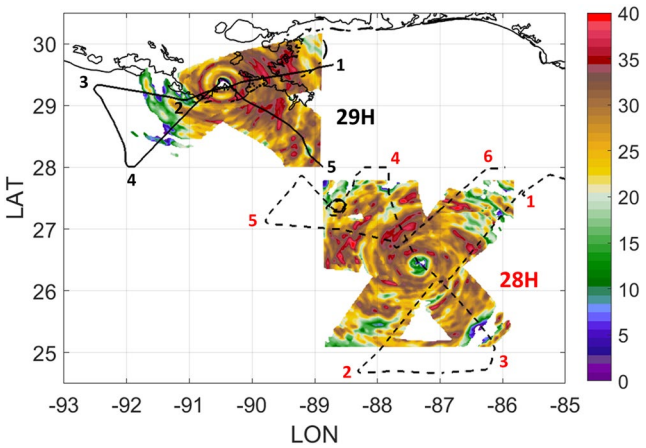

Figure 1. Radar reflectivity (shaded, dBZ) at 4-km altitude obtained from merged analyses of tail Doppler radar on the P-3 aircraft during the 28H and 29H missions (labeled). Flight tracks for each mission are overlain, with dashed (solid) lines denoting the flight track for 28H (29H). Numbers on each flight track denote initial point, key turn points, and final point for each pattern, with red (black) numbers denoting points for 28H (29H). Note that the reflectivity image is taken from the midpoint of each flight pattern, so, for example, line 1–2 from 28H does pass through the tropical cyclone center, even if it is not depicted as such in this image.

2. Case Description

Ida was declared a tropical depression at 1200 UTC on 24 August as it tracked toward the northwest in the Caribbean (Beven et al., 2022), reaching western Cuba as a 70-kt hurricane. Once it emerged into the southeastern Gulf of Mexico Ida began to strengthen rapidly, intensifying from 70 to 130 kt in the 24-hr period from 1200 UTC 28 August to 1200 UTC 29 August. By the end of this period of rapid intensification, Ida was southwest of the mouth of the Mississippi River. A continued northwest motion brought Ida inland near Port Fouchon, Louisiana, at 1655 UTC 29 August.

NOAA P-3 aircraft N42RF (hereafter N42) sampled Ida during its track across the Gulf of Mexico up to, and including, landfall. The focus of the analysis in this study will be on the final two missions of N42 into Ida. Flight tracks for these missions are shown in Figure 1. The first mission shown here, with mission ID 20210828H (hereafter 28H), occurred from 1955 UTC 28 to 0156 UTC 29 August, when Ida was in the eastern Gulf of Mexico and ∼300 km prior to landfall. During this time Ida was tracking toward the northwest at 14 kt and was experiencing 850–200 hPa vertical shear of ∼5 kt with a heading toward the east-northeast. The mission consisted of a set of radial passes through the center of Ida at different azimuthal locations, beginning and ending in the northeast quadrant. The second mission, 20210829H (hereafter 29H), occurred during landfall from 1703 UTC to 2304 UTC 29 August. This mission began with a flight leg paralleling, and just offshore, the southeast coast of Louisiana, flying inbound to the center from the east-northeast, through the center as Ida was making landfall, and continued outbound from the center toward the west-southwest. This leg, extending from points 1 to 2 from 29H as labeled in Figure 1, is termed a "coastal run," and it will be used to examine variations in offshore and onshore flow structures later. The aircraft then turned about 30° to the right (heading west-northwest), continuing to parallel the coast, but remaining offshore, until reaching point 3, where the aircraft then turned to fly away from the coast. At that point another inbound leg was flown toward the center in the southwest quadrant, followed by an outbound leg in the southeast quadrant before finishing its pattern well-removed to the southeast of the TC center. During the landfall mission Ida was tracking toward the north-northwest at a slower translation speed, and the vertical shear had increased slightly to ∼8 kt with a heading toward the east-southeast.

3. Results

Plots of radar reflectivity from the airborne radar from 28H to 29H (cf. Figure 1) show the well-developed inner core of Ida during the two missions. Ida's eye during the 28H mission was large, with a radar-defined diameter of ∼60 km and broad swaths of high reflectivity and heavy rainfall in all quadrants of the TC. For the 29H mission, Ida's eye had contracted to ∼30 km diameter. There was also an indication of an outer eyewall in the reflectivity field at ∼60 km radius from the TC center. Additional rainband activity was apparent further outward on the east side of the TC. On the west and southwest side, reflectivity outside the inner core was less widespread, possibly indicating coverage limitations or the effect of continental air entraining into the system on the offshore-flow side of the storm.

Plots of earth-relative tangential wind at 0.5 and 2 km altitude (defined as within and at the top of the TCBL, respectively (Zhang et al., 2011)) from the three-dimensional radar analyses during both 28H and 29H are shown in Figure 2. The increase in tangential winds associated with Ida's intensification up to landfall is clearly seen here. Of particular interest, however, is the azimuthal location of peak tangential winds at each altitude. For 28H, when Ida was over open water, the peak wind speeds are located in the eyewall north-northeast of the TC center within the TCBL (i.e., 0.5 km). The peak winds at the top of the TCBL (i.e., 2 km) are rotated slightly upwind, northeast of the TC center at this time. During 29H, when Ida was making landfall, there is a significant change in the azimuthal location of the peak tangential winds. Within the TCBL the strongest winds are to the south and southeast of the TC center, with an azimuthal shift of >90° clockwise of the location during 28H. The direction of the storm motion heading (vertical shear) changed by ∼10 (30) degrees between 28H and 29H (cf. arrows in Figures 2c and 2d), so the shift in the azimuthal location of the peak tangential winds does not appear to be driven, at least primarily, by changes in storm motion or vertical shear direction. Rather, the change in the azimuthal

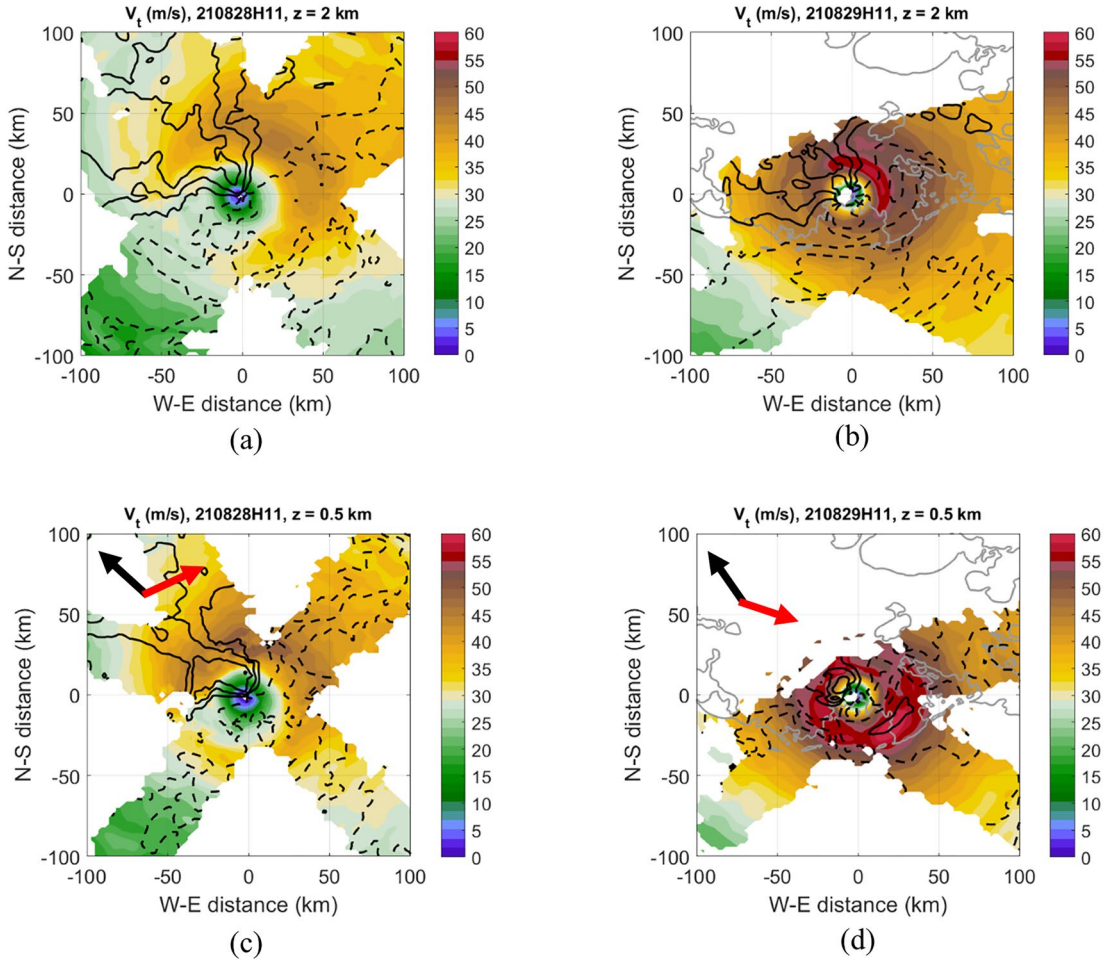

Figure 2. Earth-relative tangential wind (shaded, m s^{-1}) and radial wind (contour, m s^{-1}, solid (dashed) lines denote outflow (inflow), 3 m s^{-1} intervals) at 2 km altitude (top of tropical cyclone boundary layer (TCBL)) for (a) 28H and (b) 29H missions. Tangential and radial winds at 0.5 km altitude (within TCBL) also shown for (c) 28H and (d) 29H missions. Black (red) arrows in (c) and (d) denote storm motion (vertical shear) heading during each mission.

location of TCBL tangential winds at landfall is likely due to the adjustment of the winds as they exit the higher roughness values over land to the lower roughness over water on the offshore-flow (i.e., west) side of the TC, similar to that shown in HN22. At the top of the TCBL, the strongest winds remain to the northeast of the TC center, extending from the coast to locations well inland.

Characteristics of the radial flow within the TCBL are shown in the Doppler profile analyses in Figure 3. Figure 3a shows vertical cross sections in the lowest 2 km for radial flow along a southwest/northeast-oriented radial pass during 28H. The maximum inflow on this pass (greater than 15 m s^{-1}) is seen in the leg in the northeast quadrant. This location is to the right of the storm motion heading and to the left of the vertical shear heading, an orientation consistent with previous studies relating boundary-layer inflow and storm motion/vertical shear. Figure 3b shows a similar profile, but along the coastline (during the "coastal run" leg, from point 1–2 shown in Figure 1) during 29H. Now the radial inflow has shifted and is maximized on the west (offshore-flow) side of the TC, located ~40–50 km from the TC center, where values of peak inflow are ~20 m s^{-1}. On the east (onshore-flow) side, inflow magnitude is about half of that seen on the offshore-flow side at similar radii, though there is a weaker local maximum of inflow at about 80 km, likely associated with the outer eyewall seen in Figure 1. This relationship between the peak radial inflow in the offshore versus onshore-flow sides of the TC is consistent with HN22, who argued that the increase in the radial inflow in the offshore flow is attributed to the sudden decrease in frictional stress once the highly agradient flow crosses the coastline.

A depiction of the azimuthal variation of TCBL inflow strength, and how it varies from 28H to 29H, is shown in Figures 3c and 3d. Here the radial inflow is averaged within predefined boxes that include the RMW and between

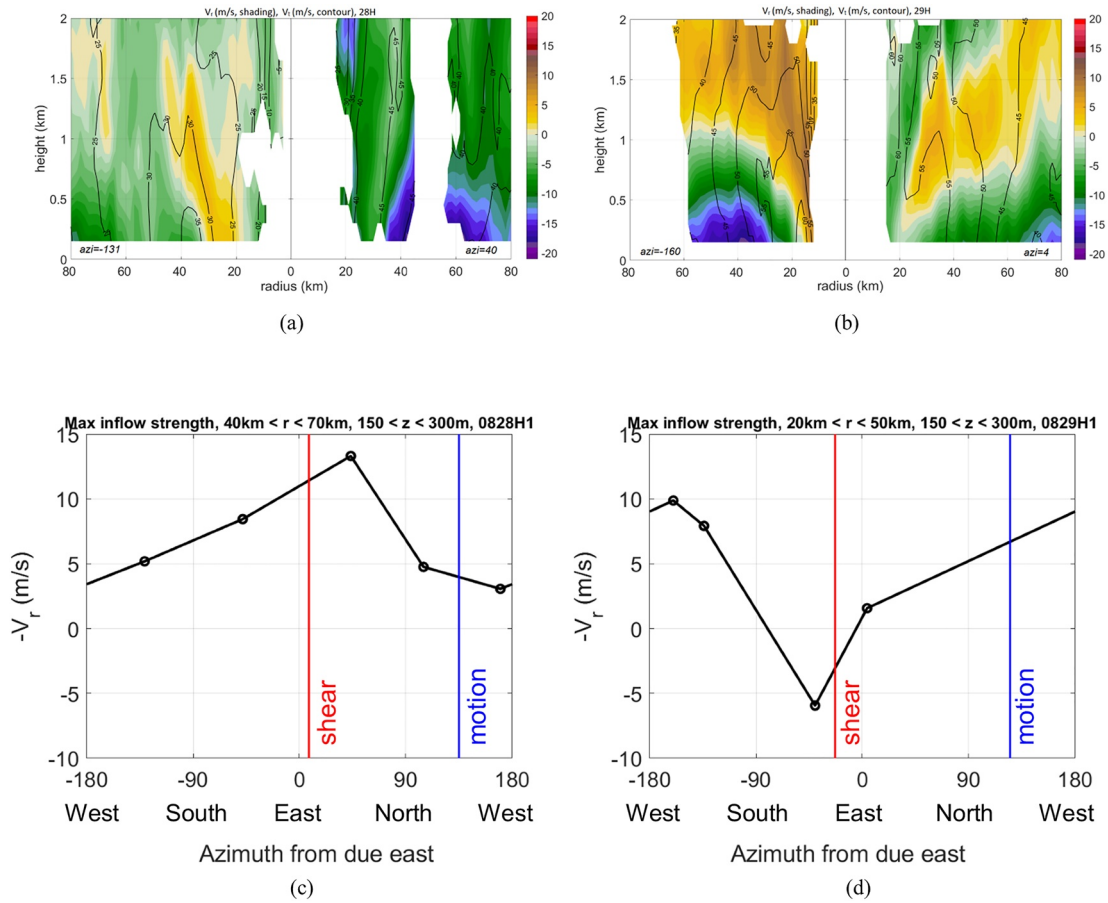

Figure 3. (a) Earth-relative tangential wind (contour, m s^{-1}) and radial wind (shaded, m s^{-1}) from southwest/northeast-oriented profile analysis from tail Doppler radar during 28H (points 1–2 in Figure 1). (b) As in (a), but for the coastal run during 29H (points 1–2 in Figure 1). (c) Azimuthal variation of areally averaged near-surface radial inflow (see text for calculation details; positive values denote inflow) for radial passes during 28H. Storm motion and vertical shear heading denoted. (d) as in (c), but for 29H. The "azi" labels in (a) and (b) denote mathematical angle, with, for example, 0 = to the east, 45 = to the northeast, −135 = to the southwest, etc.

150 and 300 m of the profile analysis for each radial pass through the TC center for both missions. These values are then plotted as a function of azimuth, with the TC motion and vertical shear heading vectors included for reference. During 28H the peak radial inflow in the lowest 150–300 m layer is located in the northeast portion of the TC, to the east (right) of the storm motion vector and to the west (left) of the vertical shear vector. Such an orientation of inflow with respect to the TC motion and shear vectors over open water is consistent with the studies mentioned earlier and shown in Figure 3a. For 29H, the orientation of radial inflow changes significantly. The strongest inflow now is on the west side of the storm. In terms of its orientation relative to the motion and shear vectors, the peak inflow in the TCBL is nearly opposite the shear vector and located about 90° to the left of the motion vector—orientations at odds with the expected azimuthal location over open water based on motion and shear considerations alone. The peak inflow is located on the offshore-flow side of the TC. Such an orientation is consistent with HN22's results, and suggests that landfall impacts, resulting from changes in the roughness length as air moves from over-land to over-water exposures, take on a greater significance in governing inflow structure than with TC motion and shear. The increase in inflow between 28H and 29H on the west and southwest sides of the storm—from about 5 m s^{-1} during 28H to 8–10 m s^{-1} during 29H—provide a potential explanation for the azimuthal location of the peak tangential winds in the southeast quadrant during 29H. The greater inward advection of angular momentum in the stronger inflow within the TCBL on the west and southwest sides during 29H lead to an enhancement in the tangential wind at the top of the TCBL downwind; that is, in the southeast quadrant, again consistent with HN22.

The variation of tangential and radial flow with height and azimuth for 28H and 29H is shown in azimuth-height transects ("curtain plots" in HN22) in Figure 4 using the three-dimensional Doppler radar analyses. Here the tangential and radial wind is averaged in a curtain of 30 km radial width around the TC center, with the inner radius

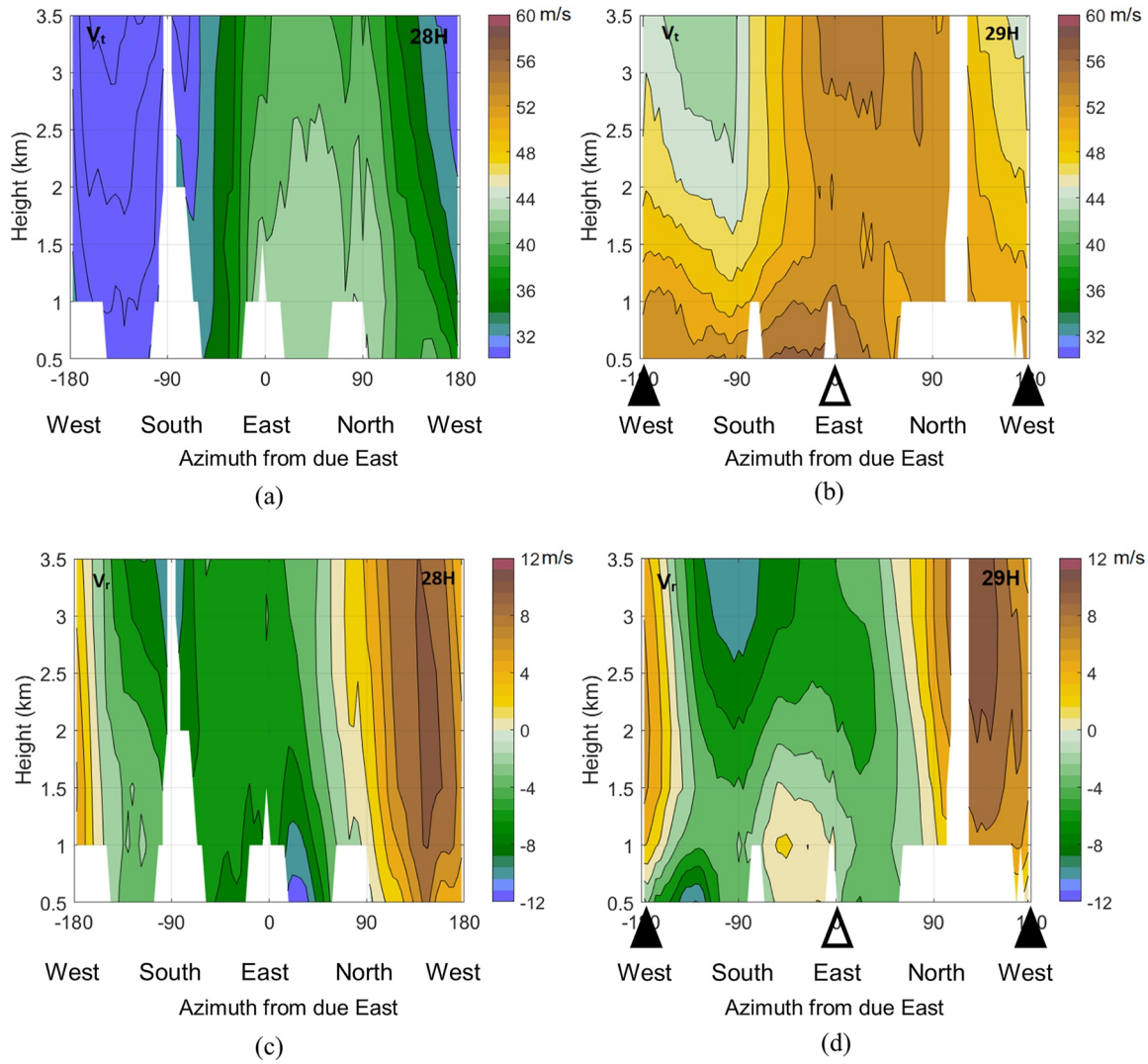

Figure 4. Azimuth-height plots (see text for calculation details) of earth-relative tangential winds (shaded, m s^{-1}) for (a) 28H and (b) 29H. (c) As in (a), but for earth-relative radial winds (shaded, m s^{-1}, negative values denote inflow). (d) As in (c), but for 29H. Triangles in (b) and (d) denote locations of coastline, with filled (unfilled) triangles denoting offshore (onshore) flow.

corresponding to the 2-km RMW that thus includes flow features at and outside the RMW, similar to HN22. Over open water, the tangential wind shows a clear wavenumber-1 pattern, with the peak values uniformly located in the northeast quadrant, from 0.5 to 3.5 km altitude. The radial flow shows a similar wavenumber-1 type pattern, with strongest inflow above the TCBL located south of the TC center and within the TCBL located east-northeast of the TC center. At landfall, the tangential and radial inflow maxima remain at the same location above the TCBL altitude as 28H. However, the locations of the maxima within the TCBL have both shifted, with the tangential wind maximum shifting from the northeast quadrant in 28H to the southeast quadrant in 29H, and the radial inflow maximum shifting from the east side in 28H to the southwest quadrant in 29H. The depth of the changes in tangential and radial flow are ~1–1.5 km, suggesting this is the depth over which the frictional effects on radial and tangential flow are dominant.

4. Discussion

The results shown here explore the structure and evolution of the TCBL during landfall. Many of the structures seen from airborne Doppler radar during Ida's landfall are similar to those shown in HN22. In particular, the strongest tangential flow is located on the onshore-flow side within and above the TCBL (cf. Figures 2 and 4). Peak radial inflow during landfall in the TCBL is located at and just downwind of the offshore-flow (cf. Figures 3

and 4), and the location of peak inflow shifts downwind, further offshore, with height above the TCBL (cf. Figure 4).

The relationship between the tangential and radial inflow peaks during Ida's landfall suggests a similar set of processes as HN22. The peak in radial inflow in the offshore flow is likely related to the sudden decrease in frictional stress when the agradient flow crosses the coastline. Enhanced advection of angular momentum by this inflow forces a strengthening of the supergradient jet near the top of the TCBL, downwind of the peak inflow. Such a relationship is seen by the downwind rotation of the azimuthal location of peak inflow and tangential wind (cf. Figures 4b and 4d). The vertical structure of the wind asymmetries (cf. Figure 4) shows the depth over which these wind field modifications occur. Prior to landfall, the inflow peak occurs on the east-northeast side of the storm. During landfall, the inflow peak shifts to the west (offshore) side of the TC. This shift extends up to 1–1.5 km altitude. The depth over which this shift occurs is generally consistent with the TCBL depth as defined by the turbulent kinetic energy field found in HN22.

While many of the results shown here support the results from HN22, there are ways that the results differ. The location of peak tangential wind in Ida at the top of the TCBL is in the northeast quadrant at landfall (cf. Figures 2 and 4). This location is inland, contrasting with the results from HN22, who showed that the tangential wind peak at the top of the TCBL is located in the right-rear quadrant relative to landfall; that is, offshore. It is not clear what the reason is for this difference. The TCs in both studies were of similar intensity (∼140 kt in HN22 and 125 for Ida). The roughness length of the swampy marshlands of the Louisiana coast is ∼0.05 cm, while the roughness lengths used in HN22 ranged between 5 and 50 cm. The sensitivity tests in HN22 showed that increasing the inland roughness length led to stronger inflow in the offshore flow, stronger inward advection of angular momentum, and more supergradient flow at the top of the TCBL in the offshore quadrants. With a much smaller roughness length for Ida, the inward advection of angular momentum and supergradient flow may have been weaker than HN22, though that still does not explain why the maximum in tangential wind was seen further downstream compared with HN22's results.

It should also be noted that the coastline of Louisiana, with its swampy marshlands, bays, and highly nonlinear coast, complicates direct comparisons with the linear, uniform coastline in HN22. One example of this complication is the fact that a portion of the 29H profile shown in Figure 3 is over land. Much of the east side of the profile (the "onshore flow" side) is along the coastline or crosses the low-lying, swampy peninsula. It is thus not a perfect comparison with the strictly linear coastline in HN22. However, because the coast here is low-lying and flat, and much of the flow upstream here is over water, it is reasonable to consider this as onshore flow at the transition between water and land. Additional data sets, with more clearly defined and linear coastlines, would enhance the analysis.

The analysis shown here extends upon that shown in HN22 by highlighting the changing importance of various physical processes in governing the structure of surface wind asymmetries prior to and during landfall. The location of the peak tangential wind and inflow is on the northeast side of Ida prior to landfall—to the right of the storm motion vector and to the left of the vertical shear vector, consistent with past studies examining the relationship between storm motion, vertical shear, and surface wind asymmetries. As Ida makes landfall, the location of the asymmetries shifts, indicating the dominant effect of frictional differences in governing the structure of asymmetries in the wind field within and at the top of the TCBL at landfall. While HN22 did include storm translation and vertical wind shear in their study, the shear magnitude was low (5 m s^{-1}), and the shear direction was oriented opposite of the motion vector, while the shear vector for Ida was perpendicular to the motion vector.

The results shown also extend on HN22 by providing observations of the three-dimensional structure and evolution of the wind field. HN22 uses buoy observations to compare inflow angles with their simulations. These buoys are fixed points in space, though they do provide time continuity. By contrast, the radar observations show a fully three-dimensional field (subject to presence of scatterers), though these fields are essentially "snapshots" in time. Ideally, a combination of these types of observing systems would provide both spatial coverage and temporal continuity.

Additional cases, including more aircraft missions sampling TCs with a similar "coastal run" pattern during landfall, are needed to assess the robustness of the results shown here. The analyses from the airborne radar also only provide snapshots over the time period required to complete the "coastal run" sampling (i.e., about 45 min), effectively smoothing out smaller-scale features that likely arise from the complex topography. The

use of ground-based radar, with ~6-min volume scans, provides an opportunity to capture these features and, combined with airborne data sets, can provide a more comprehensive analysis of TCBL structure and evolution during landfall. An incorporation of land-based observational systems, similar to those studies described above, could therefore fill in gaps in coverage from the aircraft and provide observations of roll vortices, eye-eyewall mesovortices, and convective downdrafts and associated gusts to provide an unprecedented picture of the structure and evolution of the TCBL wind field and turbulent kinetic energy prior to, during, and after landfall.

Data Availability Statement

The observational data used in this paper can be accessed through https://www.aoml.noaa.gov/2021-hurricane-field-program-data/#ida.

Acknowledgments
This work was supported by NOAA Base Funds and ONR TCRI Grant funds (with Award N00014-20-1-2071). Jun Zhang also acknowledges supports from Grants NA21OAR4590370, NA22OAR4590178, and NA22OAR4050669D, and National Science Foundation (NSF) Awards 2228299 and 2211308.

References

Ahern, K., Bourassa, M. A., Hart, R. E., Zhang, J. A., & Rogers, R. F. (2019). Observed kinematic and thermodynamic structure in the hurricane boundary layer during intensity change. *Monthly Weather Review*, *147*(8), 2765–2785. https://doi.org/10.1175/MWR-D-18-0380.1

Alford, A. A., Biggerstaff, M. I., Carrie, G. D., Schroeder, J. L., Hirth, B. D., & Waugh, S. M. (2019). Near-surface maximum winds during the landfall of Hurricane Harvey. *Geophysical Research Letters*, *46*(2), 973–982. https://doi.org/10.1029/2018GL080013

Alford, A. A., Zhang, J. A., Biggerstaff, M. I., Dodge, P., & Bodine, D. J. (2020). Transition of the hurricane boundary layer during the landfall of Hurricane Irene (2011). *Journal of the Atmospheric Sciences*, *77*(10), 3509–3531. https://doi.org/10.1175/jas-d-19-0290.1

Bell, M. M., & Montgomery, M. T. (2008). Observed structure, evolution, and potential intensity of category 5 Hurricane Isabel (2003) from 12 to 14 September. *Monthly Weather Review*, *136*(6), 2023–2046. https://doi.org/10.1175/2007MWR1858.1

Beven, J. L., Hagen, A., & Berg, R. (2022). National hurricane center tropical cyclone report: Hurricane Ida (26 August–1 September 2021). Report AL092021. 163. https://www.nhc.noaa.gov/data/tcr/AL092021_Ida.pdf

Bryan, G. H. (2012). Effects of surface exchange coefficients and turbulence length scales on the intensity and structure of numerically simulated hurricanes. *Monthly Weather Review*, *140*(4), 1125–1143. https://doi.org/10.1175/mwr-d-11-00231.1

Cione, J. J., Kalina, E. A., Zhang, J. A., & Uhlhorn, E. W. (2013). Observations of air–sea interaction and intensity change in hurricanes. *Monthly Weather Review*, *141*(7), 2368–2382. https://doi.org/10.1175/mwr-d-12-00070.1

Emanuel, K. A. (1986). An air-sea interaction theory for tropical cyclones. Part I: Steady-state maintenance. *Journal of the Atmospheric Sciences*, *43*(6), 585–605. https://doi.org/10.1175/1520-0469(1986)043<0585:aasitf>2.0.co;2

Emanuel, K. A. (1995). Sensitivity of tropical cyclones to surface exchange coefficients and a revised steady-state model incorporating eye dynamics. *Journal of the Atmospheric Sciences*, *52*(22), 3969–3976. https://doi.org/10.1175/1520-0469(1995)052<3969:sotcts>2.0.co;2

Emanuel, K. A. (1999). Thermodynamic control of hurricane intensity. *Nature*, *401*(6754), 665–669. https://doi.org/10.1038/44326

Giammanco, I. M., Schroeder, J. L., & Powell, M. D. (2012). GPS dropwindsonde and WSR-88D observations of tropical cyclone vertical wind profiles and their characteristics. *Weather and Forecasting*, *28*(1), 77–99. https://doi.org/10.1175/waf-d-11-00155.1

Hirth, B. D., Schroeder, J. L., Weiss, C. C., Smith, D. A., & Biggerstaff, M. I. (2012). Research radar analyses of the internal boundary layer over Cape Canaveral, Florida, during the landfall of Hurricane Frances (2004). *Weather and Forecasting*, *27*(6), 1349–1372. https://doi.org/10.1175/WAF-D-12-00014.1

Hlywiak, J., & Nolan, D. S. (2022). The evolution of asymmetries in the tropical cyclone boundary layer wind field during landfall. *Monthly Weather Review*, *150*(3), 529–549. https://doi.org/10.1175/MWR-D-21-0191.1

Jaimes, B., Shay, L. K., & Uhlhorn, E. W. (2015). Enthalpy and momentum fluxes during Hurricane Earl relative to underlying ocean features. *Monthly Weather Review*, *143*(1), 111–131. https://doi.org/10.1175/MWR-D-13-00277.1

Kepert, J. (2001). The dynamics of boundary layer jets within the tropical cyclone core. Part I: Linear theory. *Journal of the Atmospheric Sciences*, *58*(17), 2469–2484. https://doi.org/10.1175/1520-0469(2001)058<2469:TDOBLJ>2.0.CO;2

Kepert, J., & Wang, Y. (2001). The dynamics of boundary layer jets within the tropical cyclone core. Part II: Nonlinear enhancement. *Journal of the Atmospheric Sciences*, *58*(17), 2485–2501. https://doi.org/10.1175/1520-0469(2001)058<2485:TDOBLJ>2.0.CO;2

Klotz, B. W., & Jiang, H. (2017). Examination of surface wind asymmetries in tropical cyclones. Part I: General structure and wind shear impacts. *Monthly Weather Review*, *145*(10), 3989–4009. https://doi.org/10.1175/MWR-D-17-0019.1

Kosiba, K. A., & Wurman, J. (2014). Finescale dual-Doppler analysis of hurricane boundary layer structures in Hurricane Frances (2004) at landfall. *Monthly Weather Review*, *142*(5), 1874–1891. https://doi.org/10.1175/MWR-D-13-00178.1

Lorsolo, S., Schroeder, J. L., Dodge, P., & Marks, F. (2008). An observational study of hurricane boundary layer small-scale coherent structures. *Monthly Weather Review*, *136*(8), 2871–2893. https://doi.org/10.1175/2008MWR2273.1

Ming, J., Liu, R., Zhang, J. A., & Rogers, R. F. (2022). The shear-relative variation of inflow angle and its relationship to tropical cyclone intensification. *Journal of Geophysical Research: Atmospheres*, *127*(16), e2022JD037280. https://doi.org/10.1029/2022JD037280

Ming, J., Zhang, J. A., & Rogers, R. F. (2015). Typhoon boundary layer structure from dropsonde composites. *Journal of Geophysical Research: Atmospheres*, *120*(8), 3158–3172. https://doi.org/10.1002/2014JD022640

Ming, J., Zhang, J. A., Rogers, R. F., Marks, F. D., Wang, Y., & Cai, N. (2014). Multiplatform observations of boundary layer structure in the outer rainbands of landfalling typhoons. *Journal of Geophysical Research: Atmospheres*, *119*(13), 7799–7814. https://doi.org/10.1002/2014JD021637

Montgomery, M. T., Zhang, J. A., & Smith, R. K. (2014). An analysis of the observed low-level structure of rapidly intensifying and mature Hurricane Earl (2010). *Quarterly Journal of the Royal Meteorological Society*, *140*(684), 2132–2146. https://doi.org/10.1002/qj.2283

Ooyama, K. V. (1969). Numerical simulation of the life cycle of tropical cyclones. *Journal of the Atmospheric Sciences*, *26*(1), 3–40. https://doi.org/10.1175/1520-0469(1969)026<0003:nsotlc>2.0.co;2

Reasor, P., Rogers, R. F., & Lorsolo, S. (2013). Environmental flow impacts on tropical cyclone structure diagnosed from airborne Doppler radar composites. *Monthly Weather Review*, *141*(9), 2949–2969. https://doi.org/10.1175/mwr-d-12-00334.1

Rogers, R. F., Lorsolo, S., Reasor, P., Gamache, J., & Marks, F. D., Jr. (2012). Multiscale analysis of tropical cyclone kinematic structure from airborne Doppler radar composites. *Monthly Weather Review*, *140*(1), 77–99. https://doi.org/10.1175/mwr-d-10-05075.1

Rogers, R. F., & Uhlhorn, E. (2008). Observations of the structure and evolution of surface and flight-level wind asymmetries in Hurricane Rita (2005). *Geophysical Research Letters*, *35*(22), L22811. https://doi.org/10.1029/2008GL034774

Sanger, N. T., Montgomery, M. T., Smith, R. K., & Bell, M. M. (2014). An observational study of tropical cyclone spinup in Supertyphoon Jangmi (2008) from 24 to 27 September. *Monthly Weather Review*, *142*(1), 3–28. https://doi.org/10.1175/MWR-D-12-00306.1

Shapiro, L. J. (1983). The asymmetric boundary layer flow under a translating hurricane. *Journal of the Atmospheric Sciences*, *40*(8), 1984–1998. https://doi.org/10.1175/1520-0469(1983)040<1984:TABLFU>2.0.CO;2

Shay, L. K., Goni, G. J., & Black, P. G. (2000). Effects of a warm oceanic feature on Hurricane Opal. *Monthly Weather Review*, *128*(5), 1366–1383. https://doi.org/10.1175/1520-0493(2000)128<1366:EOAWOF>2.0.CO;2

Smith, R. K., Kilroy, G., & Montgomery, M. T. (2021). Tropical cyclone life cycle in a three-dimensional numerical simulation. *Quarterly Journal of the Royal Meteorological Society*, *147*(739), 3373–3393. https://doi.org/10.1002/qj.4133

Smith, R. K., & Montgomery, M. T. (2016). The efficiency of diabatic heating and tropical cyclone intensification. *Quarterly Journal of the Royal Meteorological Society*, *142*(698), 2081–2086. https://doi.org/10.1002/qj.2804

Smith, R. K., Montgomery, M. T., & Van Sang, N. (2009). Tropical cyclone spin-up revisited. *Quarterly Journal of the Royal Meteorological Society*, *135*(642), 1321–1335. https://doi.org/10.1002/qj.428

Sun, Z., Zhang, B., Zhang, J. A., & Perrie, W. (2019). Examination of surface wind asymmetry in tropical cyclones over the northwest Pacific Ocean using SMAP observations. *Remote Sensing*, *11*(22), 2604. https://doi.org/10.3390/rs11222604

Ueno, M., & Bessho, K. (2011). A statistical analysis of near-core surface wind asymmetries in typhoons obtained from QuikSCAT data. *Journal of the Meteorological Society of Japan. Series II*, *89*(3), 225–241. https://doi.org/10.2151/jmsj.2011-304

Uhlhorn, E. W., Klotz, B. W., Vukicevic, T., Reasor, P. D., & Rogers, R. F. (2014). Observed hurricane wind speed asymmetries and relationships to motion and environmental shear. *Monthly Weather Review*, *142*(3), 1290–1311. https://doi.org/10.1175/MWR-D-13-00249.1

Wadler, J. B., Zhang, J. A., Rogers, R. F., Jaimes, B., & Shay, L. K. (2021). The rapid intensification of Hurricane Michael (2018): Storm structure and the relationship to environmental and air-sea interactions. *Monthly Weather Review*, *149*(1), 245–267. https://doi.org/10.1175/mwr-d-20-0145.1

Wurman, J., & Winslow, J. (1998). Intense sub-kilometer-scale boundary layer rolls observed in hurricane Fran. *Science*, *280*(5363), 555–557. https://doi.org/10.1126/science.280.5363.555

Zhang, J. A., Nolan, D. S., Rogers, R. F., & Tallapragada, V. (2015). Evaluating the impact of improvements in the boundary layer parameterization on hurricane intensity and structure forecasts in HWRF. *Monthly Weather Review*, *143*(8), 3136–3155. https://doi.org/10.1175/mwr-d-14-00339.1

Zhang, J. A., Rogers, R. F., Nolan, D. S., & Marks, F. D., Jr. (2011). On the characteristic height scales of the hurricane boundary layer. *Monthly Weather Review*, *139*(8), 2523–2535. https://doi.org/10.1175/mwr-d-10-05017.1

Zhang, J. A., Rogers, R. F., Reasor, P., Uhlhorn, E., & Marks, F. D., Jr. (2013). Asymmetric hurricane boundary layer structure from dropsonde composites in relation to the environmental wind shear. *Monthly Weather Review*, *141*(11), 3968–3984. https://doi.org/10.1175/mwr-d-12-00335.1

Zhang, J. A., Rogers, R. F., Reasor, P. D., & Gamache, J. (2023). The mean kinematic structure of the tropical cyclone boundary layer and its relationship to intensity change. *Monthly Weather Review*, *151*(1), 63–84. https://doi.org/10.1175/MWR-D-21-0335.1

Zhang, J. A., Rogers, R. F., & Tallapragada, V. (2017). Impact of parameterized boundary layer structure on tropical cyclone rapid intensification forecasts in HWRF. *Monthly Weather Review*, *145*(4), 1413–1426. https://doi.org/10.1175/MWR-D-16-0129.1

Zhang, J. A., & Uhlhorn, E. W. (2012). Hurricane sea surface inflow angle and an observation-based parametric model. *Monthly Weather Review*, *140*(11), 3587–3605. https://doi.org/10.1175/MWR-D-11-00339.1

Zhu, P., Zhang, J. A., & Masters, F. J. (2010). Wavelet analyses of turbulence in the hurricane surface layer during landfalls. *Journal of the Atmospheric Sciences*, *67*(12), 3793–3805. https://doi.org/10.1175/2010JAS3437.1